High resolution photon time-tagging lidar for atmospheric point cloud generation

RORY A. BARTON-GRIMLEY,[1,*] ROBERT A. STILLWELL,[2] AND JEFFREY P. THAYER[1]

[1]*University of Colorado Boulder, Ann and H.J. Smead Aerospace Engineering Sciences Department, 1111 Engineering Drive, Boulder, CO 80309, USA*
[2]*National Center for Atmospheric Research, Advanced Study Program, Earth Observing Lab, Boulder, CO 80307, USA*
[*]rory.bartongrimley@colorado.edu

Abstract: The application of time-correlated single photon counting hardware and techniques to atmospheric lidar is presented. The results establish the viability of adapting photon time-tagging techniques to atmospheric lidar systems, facilitating high-range resolution (millimeter-level precision) and dynamic system observing capabilities that address the variety of atmospheric scatterers often present in atmospheric lidar profiles. The technique is demonstrated through measurements made by a high repetition rate, low pulse energy, elastic scattering, photon counting lidar. Detection probabilities with a non-zero system dead-time are derived and tested using acquired data. Atmospheric point cloud generation and the statistical implications on data retrievals utilizing this approach are presented. The results show an ability to preserve backscattered intensities while generating photon detections at picosecond resolution from a variety atmospheric scatterers.

1. Introduction

Photon counting has been widely used in lidar remote sensing as a tool to remotely derive properties of the atmosphere from backscattered intensity profiles. This low signal-to-noise (SNR) approach has been successful with applications spanning across many atmospheric retrievals including: quantitative measurements of clouds and aerosols [1–3], water vapor mixing ratios [4, 5], upper atmospheric temperature [6], and others. A breadth of measurements are achievable with photon counting lidar systems, establishing them as multi-functional in their ability to observe a variety of phenomena and properties by a single system. However, the desire to observe highly dynamic targets at high resolutions often introduces stringent spatial and temporal requirements, which cannot be met due to the prescribed nature of most acquisition systems — the measurement dynamics can result from the nature of the target or the implemented observational method, such as aircraft or satellite based instruments. Consequently a dynamic observing capability is necessary to match the variety and variability of atmospheric scattering targets while also accounting for the inherently low probability of detection associated with photon counting experiments.

Common photon counting lidar systems rely on acquisition and detection processing schemes that bin received photons into discrete pre-allocated time intervals over a user defined altitude range. Multichannel scaler (MCS) averagers are an example of such a data acquisition system and are the photon counting equivalent of a transient recorder [7]. These units build up a histogram of detections in defined memory locations (range bins) over a time period (integration time), typically over many laser firings, before reading out an atmospheric profile. The MCS approach, albeit very successful, is limited in its description of geophysical observations by the range and time confines imposed by the prescribed binning procedure. This serves to limit the flexibility of investigation and establishes a priori what spatial and temporal scales a particular atmospheric property must have to be observable. In addition, typical range bin resolutions do not allow for

fine feature extraction and generation of single shot profiles over the full unambiguous range of the instrument at high bin resolution provides an arduous data overhead. For example, recent work by [8] gives a geophysical requirement for bounding range resolution as ~1-10 mm in order to resolve the sharpness of cloud edges, a feature lost to spatial ambiguity in typical MCS implementations. Photon time-tagging offers the ability to approach this range resolution requirement and the agility to manage the varying signals in an atmospheric lidar profile.

The approach of photon time-tagging, where individual times of each laser firing and detected photon event are recorded relative to an absolute timing reference, is rooted in nuclear decay and fluorescence spectroscopy. Leveraging decades of advances in single-photon-sensitive detectors, data acquisition electronics, and statistical methods, Time-Correlated Single Photon Counting (TCSPC) techniques have been developed by these fields [7, 9]. Implementation of TCSPC, referred to here as photon time-tagging, for Time-of-Flight (TOF) measurements has proven advantageous as it offers shot-noise limited detections of range and the ability to generate integrated backscattered intensities with picosecond system response from "hard" targets [10, 11]. The essentials of these advancements — fast response detectors, constant fraction discriminators (CFD), and fast time-to-digital converters (TDC) — allow photon time-tagging to be applied in atmospheric backscatter measurements. This technique can address the dynamic measurement resolution needs of a single, or multi-functional, atmospheric photon counting lidar.

The technique's agility in range and time allows the measurement of atmospheric backscattered intensity profiles over the system's unambiguous range with picosecond base timing resolution. In addition, configurations of a single start (laser firing) with multi-stop detections (photon events) allow measurements beyond the first scattered return, if they lie outside the system dead-time. The system dead-time defines a time period after an initial detection in which the acquisition cannot respond to subsequent photon events, and is an important consideration when implementing photon time-tagging for atmosphere profiling. System dead-time can be associated with the type of detector or the acquisition electronics, but only acquisition dead-time is considered in this paper as the photomultiplier tubes (PMTs) used for demonstration operate with essentially zero dead-time.

This paper establishes for the first time the viability of photon time-tagging for atmospheric lidar systems. It describes the probability of detection with a non-zero system dead-time, details the experimental setup and resulting data, introduces the concept of an atmospheric point cloud, and discusses the statistical implications on data retrievals utilizing this technique. The presented results show an ability to preserve backscattered intensities from the atmosphere while generating photon detections at picosecond resolution from atmospheric scatterers. The technique is demonstrated with measurements made by a high pulse repetition frequency (PRF), low pulse energy, elastic scattering, photon counting lidar.

The outline of this manuscript is as follows. The photon time-tagging technique is introduced and described in Section 2. Sample observations made with this technique are shown in Section 3. A discussion of the advantages and limitations of photon time-tagging is given in Section 4 with a conclusion presented in Section 5.

2. Photon time-tagging technique

The technological advances associated with TCSPC experiments have yielded a class of time-tagging acquisition hardware that reliably measures and processes individual photon detections with picosecond precision (millimeter scale in range through the atmosphere) and nanosecond dead-times [12]. Implementing a combination of stable crystal oscillators, CFDs, and TDCs, modern TCSPC instrumentation can simultaneously measure MHz count rates across multiple channels and retain laser synchronization information for post processing time differencing.

Three-dimensional imaging of hard targets by lidar successfully implementing TCSPC acquisition has yielded dense sub-centimeter point cloud generation [10, 13, 14] and simultaneous

estimation of backscattered intensity. Early implementations were limited to near field measurements [13], due to the short unambiguous range of the high PRF lasers used, but advanced transmitters have led to far field point cloud generation of "hard" targets [14–16]. As a product of the targeted experiments, many of these implementations relied on a temporally gated detection scheme, with a priori information on the standoff distance of the scatterer. This implementation limits the ability to build a detection profile across the full measurement range, typically desired in atmospheric sensing, and confines the probability of a detection to a specific range gate.

Atmospheric lidar applications involve volume backscattering from "soft" targets distributed continuously and non-uniformly throughout the sensed column. Range resolution within the measurement column is dictated by the overall timing resolution of the system, described by the width of the instrument response function (IRF). In typical atmospheric lidar applications, the IRF is dominated by the data acquisition timing resolution, often several nanoseconds. However, when employing photon time-tagging, the data acquisition timing resolution is on the order of picoseconds. This then emphasizes the laser pulse-width as the limiting resolution of the IRF, see the discussion in Section 4. In addition to range resolution, atmospheric lidars also experience wide ranges of signal intensities, often 5-6 orders of magnitude or more. This dynamic signal intensity represents information content of the atmospheric scatterers and therefore requires an acquisition system capable of providing signals that are linearly proportional to the backscattered intensity. Consequently applying photon time-tagging to atmospheric profiling has different considerations than previous applications to gated hard target sensing.

Single photon events with detection probabilities of much less than one per laser firing can produce highly precise time-tags, whose estimate of intensity and range improves with temporal integration [17]. For single photon events in atmospheric sensing, this is especially applicable. Due to an altitude-dependent count rate, detections across the instrument's unambiguous range can vary in detection probability from near 100% to ≪1%. Under high count rates, the probability of detection, and thus part of the atmospheric profile, can experience dead-time distortions. Theoretical models for correcting such distortions have been well established [18, 19], but are generally specific to the measurement being pursued. In the next section, system dead-time effects resulting from the photon time-tagging technique are investigated.

2.1. Detection probability - system dead-time effects

Photon detectability at any specific time is impacted by the presence of a non-zero system dead-time, backscattered signal strength, and noise. For a photon counting lidar system, the arrival of backscattered signal and noise can be modeled as a Poisson random variable [20–22]. For a Poisson process, the probability of k events in the timing bin bounded by t_1 and t_2 is

$$P(k; t_1, t_2) = \frac{\lambda^k(t_1, t_2)}{k!} \exp(-\lambda(t_1, t_2)), \tag{1}$$

where the mean value of the distribution is given as

$$\lambda(t_1, t_2) = \int_{t_1}^{t_2} [S_{RX}(t') + \xi(t')]dt' \tag{2}$$

For the case of atmospheric lidar systems discussed here, Eq. (2) at any measurement time is composed of a backscattered signal count rate, $S_{RX}(t)$, and a noise contribution, $\xi(t) = N_{SB}(t) + N_{dark}(t)$ from solar background and detector dark counts respectively. Both $S_{RX}(t)$ and $\xi(t)$ represent photon rate functions with units of counts/second evaluated over the bin width. From Eq. (1) the probability of no photon events occurring between t_1 and t_2 is given by $\exp(-\lambda(t_1, t_2))$, therefore the probability that there is at least one or more photon events in the time bin is $P(k \geq 1; t_1, t_2) = 1 - \exp(-\lambda(t_1, t_2))$. It should be noted that in photon time-tagging

the time bin width is short enough, typically tens of picoseconds, and the unambiguous range long enough that it can be considered a point.

In the presence of system dead-time, τ_D, and for some fixed time bin width, $\tau_B = t_2 - t_1$, the integer number of time bins within a dead-time period is $N_D = \lceil \tau_D / \tau_B \rceil$. Considering a single laser pulse, the system will register a detection in the j_{th} bin if the N_D bins before the j_{th} bin have not registered a detection [23]. The probability that the acquisition registers a photon event in the j_{th} bin is then

$$
\begin{aligned}
P_j &= \left[\prod_{i=j-N_D}^{j-1} P(k = 0; i) \right] P(k \geq 1; j) \\
&= \exp\left(- \sum_{i=j-N_D}^{j-1} (S_i + \xi) \right) [1 - \exp(-S_j - \xi)],
\end{aligned}
\tag{3}
$$

where it is assumed that the number of events per bin is generated by independent Poisson processes. The rate function is now expressed as the backscattered signal strength in the j_{th} bin and a constant noise term, assuming that the solar background and detector dark counts are constant over the laser's inter-pulse period (IPP) for single shot analysis.

Expansion of the first term in Eq. (3) introduces a combined expression for the dead-time weighting function for a given signal count rate, noise count rate, system dead-time, and bin width as

$$
W_j(S, \xi, N_D) = \begin{cases} 1 & N_D = 0 \\ \exp(-\xi N_D) \exp\left(-\sum_{i=j-N_D}^{j-1} S_i \right) & N_D > 0 \end{cases}
\tag{4}
$$

Separate terms describe the impact of noise and signal on the weighting function. As the system dead-time goes to zero, the summation yields the bounds $i = j > j - 1$, giving the empty set. This maximizes W_j to unity and removes dead-time effects from the estimated signal.

Combining Eqs. (3) and (4) yields the probability of detection in the j_{th} bin as

$$
P_j = W_j(S, \xi, N_D)[1 - \exp(-S_j - \xi)],
\tag{5}
$$

where the probability of one or more positive detections in the j_{th} bin is scaled by the value of W_j. When the number of events per laser firing is small, Taylor expansion of the last term in Eq. (5) approximates the expression as

$$
P_j \approx W_j(S, \xi, N_D)(S_j + \xi),
\tag{6}
$$

showing a direct relationship between the detection probability and the signal count rate.

Figure 1 shows the results of Eq. (5), with contributions by W_j and S_{RX}. Modeling of the single-shot backscattered signal was performed utilizing the Stokes Vector Lidar Equation formulation from [24] and the instrument parameters listed in Table 1, which are the actual parameters for the lidar system used in Section 3 for demonstration. The signal count rates were generated for a vertically pointing lidar with a 4 mm range resolution (27 ps timing resolution) and a bounding altitude equal to the instrument's unambiguous range of ~ 10.49 km. A 100 kHz Poisson noise source is assumed, re-sampled to the IPP of the laser at 4 mm bins. The case of randomly oriented particles and single scattering was assumed using the scattering matrix described in [25, 26] combined with a clear air depolarization value of $\delta = 0.0036$ [27, 28]. The NRLMSISE-00 atmospheric model was used to generate height-dependent atmospheric density values, providing estimates of the volume backscatter coefficient and path extinction by molecular

scattering. The simulation results were scaled by an optical efficiency factor to match the actual values measured by the demonstration instrument to generate realistic single-shot probabilities.
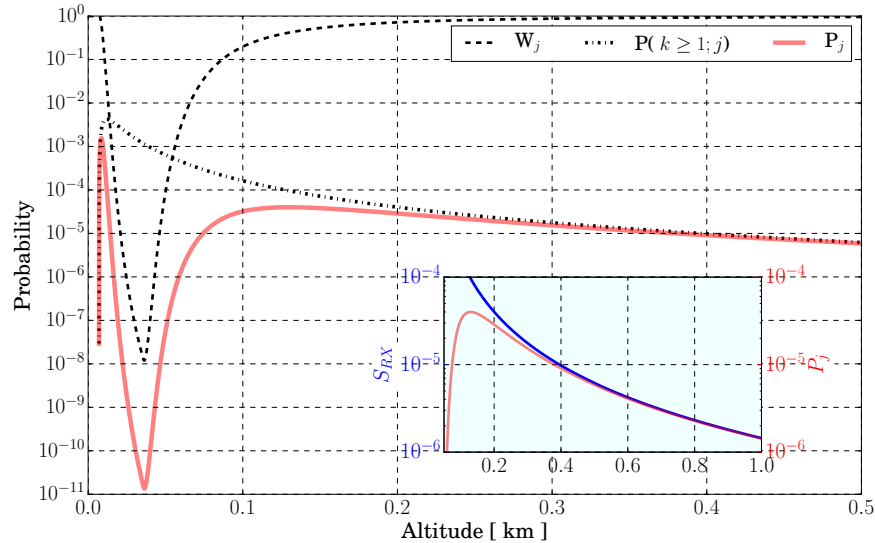

Fig. 1. Simulated curves for the individual terms of Eq. (5). The dashed line shows the weighting function W_j - the null detection probability within N_D bins prior to the j_{th} bin, the dot dashed line shows the probability of one or more detections in the j_{th} bin, $P(k \geq 1, j_{th})$, and the red line shows the combined probability P_j. The figure inset shows the effects of dead-time distortion by comparing the shape of P_j, red line, and S_{RX}, blue line.

Figure 1 demonstrates the interplay between backscattered signal strength, the $k = 0$ probability in the prior N_D bins, and the $k \geq 1$ probability in the j_{th} bin. High signal strengths in the lower atmosphere result in W_j being less than one, as there is a high probability of detecting a photon within prior N_D bins. As the backscattered intensity falls off with altitude, W_j increases to unity and the $k \geq 1$ probability for the j_{th} bin dominates P_j. The two curves are of opposite tendency, resulting in a peaking of the combined probability curve. The dead-time weighting function continues to contribute to the overall detection probability past this peak until it reaches unity. This behavior is similar, but distinct, from the description often attributed to the geometric overlap function of a monostatic lidar system.

The inset of Fig. 1 shows an overlay of the simulated signal, S_{RX}, and combined probability, P_j. The curves indicate that with a non-zero system dead-time the shape of P_j will deviate from the incident signal count rate if $W_j < 1$, leading to intensity distortions. At lower altitudes, where count rates are high, the integrated intensity profiles are non-linear with the backscattered signal. With the given relationship between the impinging photon rate and the acquired signal, signals outside of the linear regime can be recovered through non-linear fitting [19, 29]. The magnitude and extent of the intensity distortion directly depends on W_j.

Figure 2 shows Eq. (5) evaluated at the demonstration instrument's 4 mm range resolution with different system dead-time values. As τ_D approaches zero, detectability of count rates increases, leading to a linear detectability across a larger altitude range, i.e. expanding the linear signal dynamic range of the system. Computing the percent deviation between the signal waveform and the combined probability shows that when assuming a large system dead-time (190 ns, accurate for the counting system described in Section 3) the shape of P_j nears linearity to S_{RX} (within 1% error) at 1.0 km, whereas a shorter system dead-time of 2.5 ns (commercially available) nears
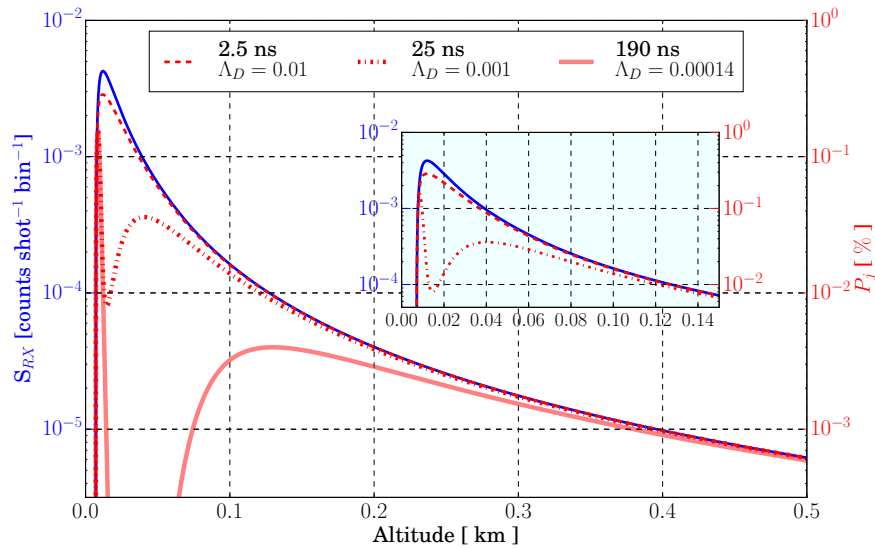
Fig. 2. P_j curves simulated with Eq. (5) and varying the system dead-time with a fixed timing resolution of 27 ps. The signal term, S_{RX}, is shown in blue. The resulting P_j curves computed with different system dead-times of: 2.5 ns (dashed), 25 ns (dot-dashed), and 190 ns (solid), shown in red. The inset zooms in to the 2.5 and 25 ns curves at low altitude.

linearity at 125 m. This improves linear signal dynamic range, and thus detectable photon rates, by nearly two orders of magnitude.

A figure of merit for signal dynamic range coverage can be defined as $\Lambda_D = 1/N_D = \tau_B/\tau_D$, which is the ratio of timing resolution to system dead-time. For a fixed bin width, Λ_D increases as system dead-time is decreased, thus maximizing W_j at a lower measurement altitude and effectively improving the linear signal dynamic range. A short system dead-time with high timing resolution is the most desirable, but not always achievable with current TCSPC acquisition units. Often, a short system dead-time is accompanied by poorer timing resolution. This simple relation can facilitate assessing trade-offs between covering a large signal dynamic range with reduced range resolution or achieving high range resolution, but over a smaller signal dynamic range. With an appropriate value of Λ_D, a given set of instrument parameters can be tuned to generate accurately modeled signal strengths that account for P_j. This provides realistic detectability estimates and defines signal dynamic range limits that adequately suit the measurement requirements.

3. Photon time-tagging observations

Photon time-tagging hardware has been incorporated into an existing lidar system to demonstrate the applicability of this technique for advancing atmospheric lidar applications. System parameters of the demonstration instrument are summarized in Table 1. This lidar transceiver was adapted from an airborne shallow water bathymetric sounder [30].

A passively Q-switched, frequency-doubled Nd:YAG microchip laser with a central wavelength of 532 nm, a PRF of 14.3 kHz, 35 mW of average power, and a full width half max (FWHM) pulse-width of <500 ps was used as the transmitter source. The PRF implemented gave the system a range ambiguity of 70 μs, ∼ 10.49 km, sufficient for lower tropospheric detections. The beam is passed through a 5X Galilean beam expander to set the outgoing divergence at 2 mrad. A half-wave plate and Glan-Thompson polarizer ensure that the transmitted light has no excess

loss in average power and a high degree of linear polarization. The beam is steered through adjustable Risley prism pairs for far field alignment. A back reflection from the steering system is directed to a commercial photodiode, providing the start signal for time correlations.

The transmit and receive channels are arranged biaxially, separated spatially so that full geometric overlap is achieved after 30 m. The backscattered photons are collected with a commercial 90 mm aperture F13.9 Maksutov-Cassegrain telescope and spatially filtered by an adjustable field stop at the telescope focus. Collected photons are spectrally filtered by 300 pm interference filter, allowing operation under high background conditions. A Glan-Taylor polarizer splits the received photons into co/cross-polarized signals relative to the transmitter, and each are focused onto separate Hamamatsu H7422P-40 PMTs. The detectors have an average dark count rate of 300 Hz and the time transient spread (TTS) was measured as approximately 280 ps, matching previously published values [7]. Detector outputs are routed to CFD/TDCs providing stop signals for post processing. The FWHM of the IRF was measured to be 530 ps, equivalent to 7.945 cm in range. The laser's temporal width dominates the convolved IRF for our PMT/CFD/TDC setup, such that the measurement resolution of the acquisition system over samples the IRF/target response function. Therefore, interpretation of the target at the TDC's millimeter range resolution cannot be realized unless the IRF is deconvolved from the signal waveform. However, there are instances where measurements of multiple targets can be attained at the TDC resolution independent from detector bandwidth and laser pulse-width, see [30].

Table 1. Summary of demonstration lidar system parameters

System Parameter	Value
Wavelength	532.00 nm
Laser Repetition Rate	14.3 kHz
Laser Pulse-Width	< 500 ps
Laser Output Energy	2.45 μJ
Transmitter Divergence	2 mrad
Transmitter Polarization	> 99% Linear Vertical
Telescope Type/Diameter	Maksutov-Cassegrain/90 mm
Receiver Field of View	Adjustable - nominally set at 2 mrad
Receiver Filter Bandwidth	300 pm FWHM
Receiver Detectors	Hamamatsu H7422P-40, 40% QE,280 ps TTS
Data Acquisition Hardware	SENSL CFD, SENSL HRMTime
Data Acquisition Dead-Time	190 ns
Minimum Acquisition Range Resolution	4 mm
System Dead-Time Metric (Λ_D)	0.00014

Initial tests were performed using independent CFD/TDCs for each start/stop channel, with 190 ns dead-time per channel. A master clock synchronized the channels at 250 kHz and the TCSPC module was configured with 27 ps timing resolution (4 mm in range), continuously

streaming all channels to the host computer. Photon detections from each receiver channel are correlated to the correct laser firing assuming all detections come from the first unambiguous range (a reasonable assumption for low average power systems profiling the troposphere with no high clouds, such as cirrus). Long term drift of the master clock is unimportant as only relative timing between laser firing and photon event are needed. The resulting data produce a real-time point cloud of photon TOF values for every photon event, with co-registered experiment detection time at 27 ps resolution.

Figure 3 illustrates an integrated signal profile generated by the lidar described in Table 1 and implementing photon time-tagging acquisition. These data represent backscattered signals received in the co-polarized channel by the zenith-directed configuration due to atmospheric molecular and particulate scattering. Total counts are displayed versus altitude over a ten second period with 4 mm acquisition range bins spatially integrated to 12 mm (Panel A) and 1 m (Panel B). The data profiles in panels A and B indicate decreasing volume scattering with altitude due to the exponential decrease in the density of molecular scattering and the inverse squared range dependence of volume scattering. The summing of counts over a larger bin width (by a factor of 100) in Panel B improves the estimate of mean counts within a bin by the square root of the total counts within that bin while sacrificing range resolution.
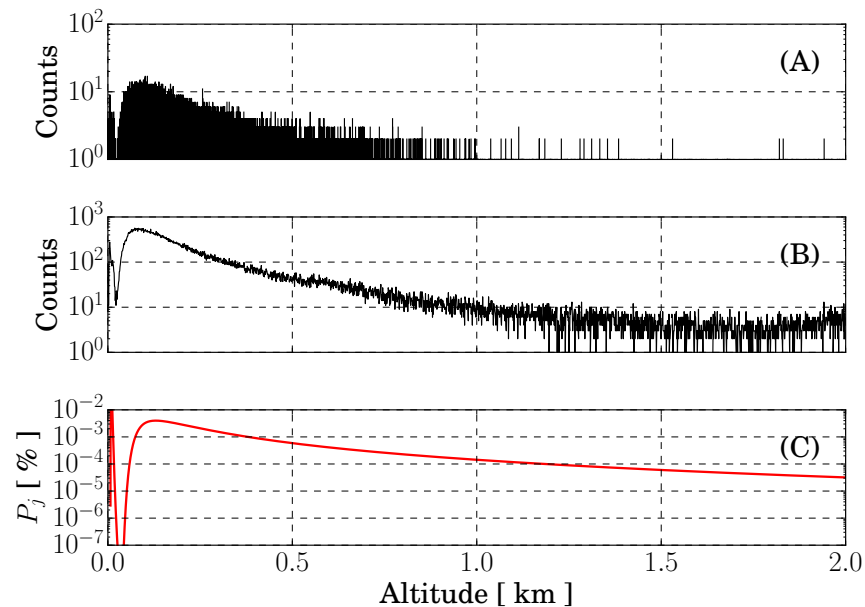

Fig. 3. Intensity profiles integrated from 10 s of raw atmospheric point cloud data at 12 mm (panel A) and 1 m (panel B) range resolution. Panel C shows the computed P_j from Fig. 1 using the instrument parameters in Table 1.

There remain challenges with photon time-tagging acquisition that were discussed in the previous section - notably the effects of non-registered photon events due to system dead-time as a function of count rate. Panel C of Fig. 3 illustrates the simulated P_j curve using the system parameters given in Table 1, a geometric overlap function, and simulated count rates determined from panels A and B. Panel C describes many of the features observed in the measurements. At low altitudes the ideal counts are high, but the observed counts are low due to the probability of having a detection prior to the observing bin - W_j is much less than one. Full geometric overlap

occurs relatively quickly, at 30 m, leaving deviations of observed counts to ideal counts above this altitude solely due to system dead-time effects. The simulated near ground spiked feature is evidence of this fact and is also observed in the data, where geometric overlap and system dead-time simultaneously influence the probability curve. This feature marks the location where the decreasing backscatter signal and the fraction of transmitter/receiver geometric overlap are such to produce signal behavior that is low and only weakly influenced by W_j. This condition is eliminated quickly as the geometric overlap increases the signal count rate and, consequently, a rapidly decreasing W_j reduces the probability of detection. According to the simulation, the weighting factor approaches unity before 1 km altitude. Thus, for altitudes below 1 km the signal intensity is distorted by the system dead-time. Per Fig. 2, reducing the system dead-time and degrading timing resolution are means to reduce distortion, resulting in a greater linear signal dynamic range and constraining systematic effects to lower altitudes.

Figure 4 illustrates the agility of the system where signals from different scatterers can be handled separately in post processing to achieve the temporal/spatial resolutions and parameter accuracy required for that particular investigation. Molecular scattering can be coarse and slow in evolution, while cloud dynamics can be fine and rapid. Both aspects can be studied by independently using a variety of post processing methods. Figure 4 shows the results for a simple SNR based dynamic binning process, where a feature threshold of SNR ≥ 3 for signals beyond 1 km, was used to select bin widths. The resulting integrated profile gives 2 m bins from 1-2.7 km, where individual diffuse aerosol scattering layers can be seen at 2, 2.3, and 2.6 km. From 2.7-3.3 km the profile structure increases bin resolution to 26 cm, capturing the sharp cloud returns. Performing dynamic signal evaluations in post processing relies on the capability of recording data at the highest resolution possible, every photon event per laser firing at the full TDC timing resolution. The demonstrated method provides equivalent raw data to a typical MCS acquisition, but at 14.3 kHz and 4 mm resolution.
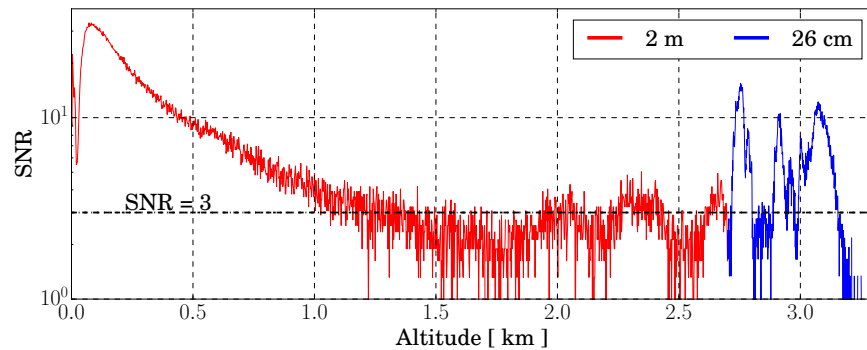

Fig. 4. Dynamically integrated intensity profile using a SNR≥3 feature filter, shown by the labeled dot-dashed line, over 10 s of accumulated photon events. The aerosol features present in the data from 1.5-2.7 km are extracted using a 2 m bin width, and the sharp cloud features from 2.7-3.3 km are extracted using a 26 cm bin width. Background signal, ξ, was computed as a geometric mean between 4-5 km.

This type of collection, per laser firing, may not be feasible for lidars utilizing MCS acquisition. Every bin within the laser's unambiguous range would be a memory location, and data recorded (zero or non-zero) over a large range (∼ 10.49 km) at high resolution (4 mm) would require unfeasible memory capacity and data transfer rates. Photon time-tagging removes this limitation by tagging only the bin occupied by a photon event per laser firing. Due to the photon counting condition of low probabilities of occurrence, resulting data transfer rates are small, as is the saved

data file. For an available commercial unit with a system dead-time of 25 ns, sustained count rates of 40 MHz with bursts upwards of 125 MHz [12] are possible. Considering that every detection is a 32 bit number, the maximum sustained transfer rate for this unit then becomes 160 MByte/sec. Given that system operation is normally tuned to a lower probability of detection to avoid pulse pile-up, the data rate can be reduced to kBytes/sec while generating single-shot atmospheric profiles, as is the case for this work. A comparable MCS system, lacking this sparse storage mechanism, would generate 150 GBytes/sec for the same measurement.

4. Discussion

A complete photon time-tagging lidar system for atmospheric applications is capable of measuring backscattered intensity, estimate range at high resolution, and operate over a broad signal range. These attributes are summarized by the overall timing resolution and system dead-time, as described by Λ_D in Section 2. The interplay between these two attributes affects the span of recorded counts that are linearly proportional to the signal intensity. The linear signal dynamic range can be extended if the system dead-time is shortened or a functional form for the system dead-time effects can be applied to the non-linear portion of the recorded signal.

Complementary to the ability to measure backscattered intensities is the high resolution ranging that the technique affords. As is often the case with photon time-tagging approaches, the range resolution is not dictated by the TDC's timing resolution, but by the IRF of the lidar system. In photon time-tagging, the detected signal waveform is the convolution of the IRF —dominated by the laser pulse-width and detector TTS as measured against a delta function target — and the target's temporal response. The detector's TTS describes statistical variability in the leading edge of the output pulse. With PMTs, the TTS is much less than the FWHM of the detector pulse-width (often an order of magnitude lower), effectively reducing the system IRF and emphasizing the laser pulse-width as the IRF limiting factor. Reduction of the lidar's IRF, through shorter laser pulse-widths and detectors with a small TTS, allows the time resolution description of the atmospheric point cloud to be increased.

Implementation of a post detector CFD serves to reduce the time ambiguity introduced by statistical pulse height variations, prevalent in PMT operations. Modern TCSPC units exhibit combined CFD and TDC root mean square timing jitters of < 10 ps [12], effectively creating a response that falls within the TDC's timing resolution and has little impact to the system's IRF. For example, the 530 ps IRF reported for the demonstration instrument is dominated by the laser pulse-width. The timing resolution of the TDC is much finer than the IRF resulting in the measurements being limited in resolution not by the timing resolution, but by the IRF.

With a more complete understanding of the photon time-tagging approach, the augmented lidar was directed vertically to acquire atmospheric backscattered signals over several hours. The profiles shown in in Fig. 3 were integrated from the post-processing of singular photon time-tags. Figure 5 illustrates the backscattered signals over time and altitude without any post processing. These data are atmospheric point clouds where every photon is assigned a time-tag with 27 ps resolution. The increased density of photons (darker shade of gray) indicates higher count rates due to greater scattering efficiency - either an increase in cross section of the scatterers, a greater concentration of the same scatterers, or both.

The point clouds show the ability of the detection scheme to acquire photon events at high temporal and spatial resolutions and capture the measurement scene dynamics. In the atmospheric point cloud, features and transitions are seen as clusters of dense returns. The backscattered signal demonstrates variability consistent with molecular, aerosol, and cloud particle scattering. The low-altitude, high-density signal is largely due to molecular scattering at close range. The band of high-density points between 2 and 3.3 km are strong and frequent photons from the base and interior of clouds. The cutoff of signal above the cloud is due to extinction of the laser energy. Diffuse scatterers with significant variability are also observed in Figs. 5 and 6, possibly
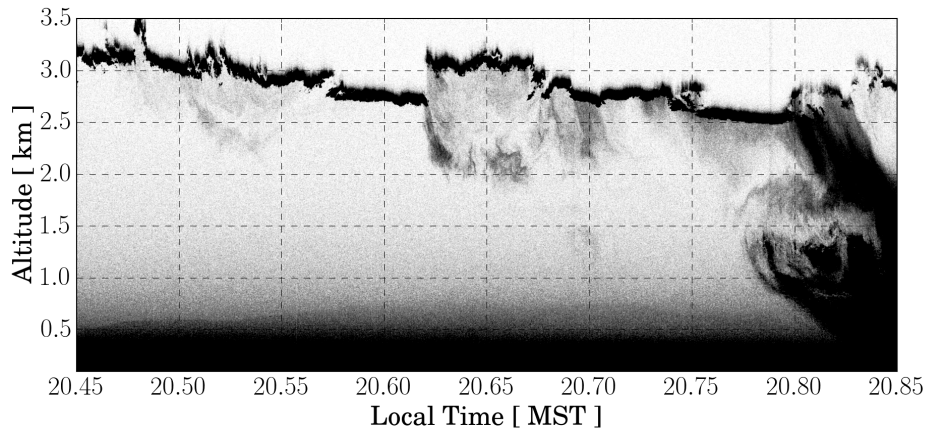
Fig. 5. Time-correlated portion of the collected atmospheric point cloud. Each photon was correlated to the associated laser firing at the full 27 ps resolution of the TDC and plotted as computed range versus collection time. The atmospheric density gradient and dense locations of returns indicative of highly reflective cloud structures and rainfall are evident.

representing evaporating rain (virga) or actual rainfall at the end of the observations.
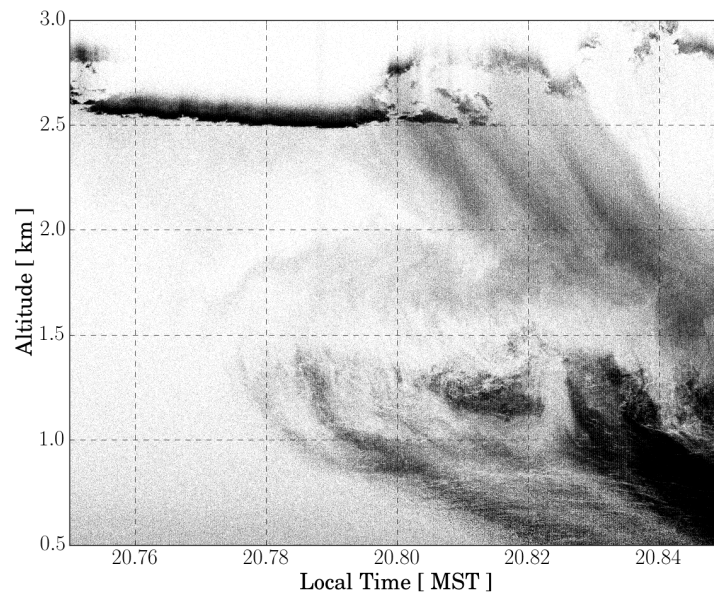

Fig. 6. Subset of Fig 5, showing zoomed in features representing dense structure amongst the Poisson distributed noise field, showing what could be virga or actual rainfall.

Figure 6 shows the ability to detect density changes in diffuse and sharp atmospheric features amongst the randomly Poisson-distributed noise field. A single co-polarized plane was used for analysis. In the case of systems employing a cross-polarization receiver channel for depolarization estimates, the crossed polarization planes will experience different time evolving count rates, typically with co-polarized producing higher count rates than cross-polarized [31]. This results in

a channel dependent W_j and P_j. However, time-tagging systems handle both regimes, as system dead-times (including detector) exist within each channel independently, not across channels, allowing cross-correlations between channels within the system dead-time [12]. Challenges arise when analyzing the signals together, often in the form of a ratio to determine scatterer-induced signal depolarization. Systematic effects can significantly impact signal depolarization [24,32,33] and such effects require careful evaluation of signal behavior. Here, the signals can be evaluated in the context of the W_j and the analysis presented in Section 2.

Scientific retrievals typically rely on inversions of integrated backscatter intensity, requiring further processing of the atmospheric point cloud. Standard techniques employ histogram generation at bin sizes greater or equal to the TDC resolution, typically driven by desired SNR. Binning is performed over a selectable number of laser firings, allowing single-shot profile generation to any multiple of the instrument's IPP. This method allows a dynamic approach to generating time series of photon detections, where the number of laser firings integrated and the desired timing resolution can be approached in a manner that best suits the science retrievals pursued. Performing an optimum search for the time and range integration scheme is then driven by the the ability to resolve features, providing agility in the final product produced. Hence photon time-tagging provides more flexibility over more traditional techniques, such as MCS. The limit on the selectable binning resolution is driven by the Nyquist criterion, where the oversampling of the signal waveform is bounded by the temporal structure of the IRF.

To demonstrate the applicability of the atmospheric point cloud for intensity based retrievals, the data from Figs. 5 and 6 were binned to 10 m vertical spatial and 10 s temporal resolutions using the methods discussed. The resolution choice was driven by the need for high SNR, 20 or above was chosen, to ensure that retrieval algorithms converged. The individual profiles were background subtracted and passed through a speckle filter to reduce the noise field. The normalized backscatter ratio was calculated using the Klett inversion technique [34]. A combination of the implemented methods can be seen in [31]. The results for the retrieved normalized backscatter ratio are shown in Fig. 7. Note that the cloud tops with low backscatter ratio are not physical, but rather an artifact of the Klett inversion used to calculate backscatter ratio.
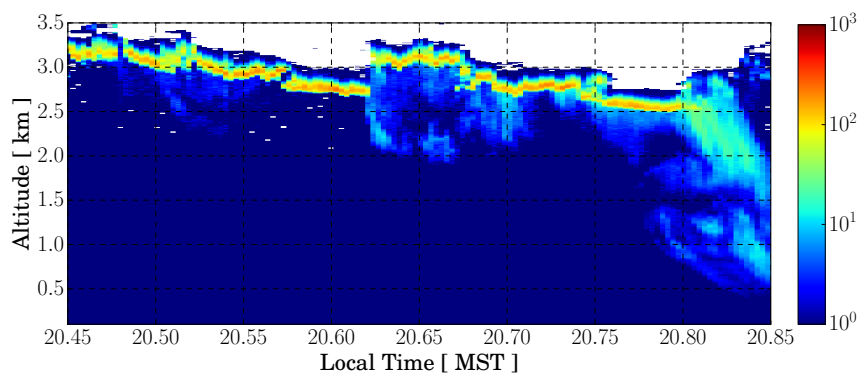

Fig. 7. Retrieved normalized backscatter ratio, computed according to [31, 34], from the atmospheric point cloud shown in Figs. 5 and 6. White areas above 3 km are locations where integrated signal fell below the SNR threshold for the retrieval algorithm.

Several of the macroscopic structures present in Figs. 5 and 6 (note that the time scales are not equal) were captured in the binning and retrieval processes, shown in Fig. 7. However, many of the finer structures, such as those in Fig. 6, become spatially ambiguous when employing these processing techniques. These traditional processing techniques serve to significantly decrease the

resolution of the photon time-tagging technique, opening opportunity for algorithm development and applications that exploit the full utility of the technique.

Multiple techniques have been developed to estimate clustered target densities, not emphasizing simultaneous intensity retrievals, amongst Poisson noise fields [35]. Methods to extract features from noise in photon limited data, utilizing traditional histogram approaches for binning structure, have been successful with the optimal estimation approach [3, 36]. However, the high resolution atmospheric point cloud opens the possibility for applying vetted image processing techniques that can maximize the usefulness of the temporal and spatial resolutions. Photon limited non-parametric Poisson intensity and density estimations have been shown in [37], and [38] show promising results reconstructing scenes using Poisson likelihood estimators. Leveraging the known Poissonian nature of photon counting lidar and the time-tagging technique, these methods provide alternative approaches, with enhanced flexibility, to working with atmospheric point clouds. Initial investigation of these methods has been performed and shown to be viable for the photon time-tagging techniques in this work.

The adaptation of TCSPC hardware to a photon-counting lidar system and the application of photon time-tagging to atmospheric sensing has been demonstrated. In addition to the demonstration discussed in this paper, the time-tagging approach was successfully implemented on an airborne platform during the 2015 NASA SARP program, the 2016 NSF/NCAR sponsored ARISTO campaign, and on a 30 Hz, 400 mJ, water vapor Raman system. The results are not be shown in this paper. The results of that work are similar to that which is presented here, and further emphasizes the added flexibility of the described photon time-tagging approach.

5. Conclusion

Implementation of the photon time-tagging technique provides an efficient method to acquire photon events, with the advantages of generating detections per laser firing at picosecond timing resolution throughout the atmospheric column. The resulting data are an atmospheric point cloud in time and range, capable of revealing fine-scale features and enabling dynamic integration. This capability can prove favorable for measurement scenarios with limited time on target due to relative platform motion, such as aircraft and spacecraft observations. Low data rate demands, due to the sparse nature of single-shot photon counting data, are also conducive to situations where high bandwidth telemetry is not possible. Furthermore, nadir viewing airborne and spaceborne lidar systems often capture both atmosphere as well as land and ocean backscattered returns [39,40]. Acquisition system flexibility would allow for such diverse scattering scenarios to be fully captured and post-processed for multi-functional retrievals requiring dynamic resolutions.

Several attributes of a photon time-tagging lidar for atmospheric applications that differ from typical atmospheric lidar systems were presented. Acquisition dead-time is an important parameter that can affect signal behavior in high count rate domains - such as occurs in the low-altitude or cloud backscattered signals. A ratio of acquisition timing resolution to dead-time was shown as a reasonable metric, see Fig. 2 for an example of dead-time induced count rate reduction, for optimizing a system's linear signal dynamic range. The discussed technique significantly reduces the IRF, which is largely driven by the laser pulse-width and the detector's timing jitter. The detected signal waveform is then a convolution between the IRF and the uniform spread of the atmospheric scatterers over the pulse width. Thus, backscattered signals recorded with picosecond timing cannot be considered independent until integration to the IRF width has been reached — approximately 500 ps, or 7.5 cm for the demonstration instrument discussed here. In this situation, a decrease in timing resolution can be afforded if the system dead-time is also reduced. Even so, centimeter range resolutions in atmospheric profiling is a new capability and can begin to contribute to fine-scale atmospheric processes associated with cloud formation, turbulence, laminae, and other phenomena. Furthermore, this technique can be applied to the wide variety of lidars often applied to atmospheric studies, such as differential absorption lidar,

Raman lidar, and resonance-fluorescence lidars, whose scattering properties may be conducive to small-scale observation or dynamic integration.

References

1. J. R. Campbell, D. L. Hlavka, E. J. Welton, C. J. Flynn, D. D. Turner, J. D. Spinhirne, V. S. S. III, and I. H. Hwang, "Full-time, eye-safe cloud and aerosol lidar observation at atmospheric radiation measurement program sites: Instruments and data processing," J. Atmospheric Ocean. Technol. **19**, 431–442 (2002).
2. M. McGill, D. Hlavka, W. Hart, V. S. Scott, J. Spinhirne, and B. Schmid, "Cloud Physics Lidar: Instrument Description and Initial Measurement Results," Appl. Opt. **41**, 3725–3734 (2002).
3. M. Hayman and S. Spuler, "Demonstration of a diode-laser-based high spectral resolution lidar (hsrl) for quantitative profiling of clouds and aerosols," Opt. Express **25**, A1096–A1110 (2017).
4. A. R. Nehrir, K. S. Repasky, and J. L. Carlsten, "Eye-safe diode-laser-based micropulse differential absorption lidar (dial) for water vapor profiling in the lower troposphere," J. Atmospheric Ocean. Technol. **28**, 131–147 (2011).
5. S. M. Spuler, K. S. Repasky, B. Morley, D. Moen, M. Hayman, and A. R. Nehrir, "Field-deployable diode-laser-based differential absorption lidar (dial) for profiling water vapor," Atmospheric Meas. Tech. **8**, 1073–1087 (2015).
6. J. P. Thayer, N. B. Nielson, R. E. Warren, and C. J. Heinselman, "Rayleigh lidar system for middle atmosphere research in the arctic," Opt. Eng. **36**, 2045–2061 (1997).
7. W. Becker, *Advanced Time-correlated Single Photon Counting Techniques* (Springer Science & Business Media, 2005).
8. M. J. Beals, J. P. Fugal, R. A. Shaw, J. Lu, S. M. Spuler, and J. L. Stith, "Holographic measurements of inhomogeneous cloud mixing at the centimeter scale," Science **350**, 87–90 (2015).
9. P. Kapusta, M. Wahl, and R. Erdmann, *Advanced Photon Counting - Applications, Methods, Instrumentation* (Springer, 2015).
10. A. McCarthy, N. J. Krichel, N. R. Gemmell, X. Ren, M. G. Tanner, S. N. Dorenbos, V. Zwiller, R. H. Hadfield, and G. S. Buller, "Kilometer-range, high resolution depth imaging via 1560 nm wavelength single-photon detection," Opt. Express **21**, 8904–8915 (2013).
11. A. M. Pawlikowska, A. Halimi, R. A. Lamb, and G. S. Buller, "Single-photon three-dimensional imaging at up to 10 kilometers range," Opt. Express **25**, 11919–11931 (2017).
12. M. Wahl, T. Röhlicke, H.-J. Rahn, R. Erdmann, G. Kell, A. Ahlrichs, M. Kernbach, A. W. Schell, and O. Benson, "Integrated multichannel photon timing instrument with very short dead time and high throughput," Rev. Sci. Instrum. **84**, 043102–043110 (2013).
13. J. S. Massa, G. S. Buller, A. C. Walker, S. Cova, M. Umasuthan, and A. M. Wallace, "Time-of-flight optical ranging system based on time-correlated single-photon counting," Appl. Opt. **37**, 7298–7304 (1998).
14. M. Henriksson, H. Larsson, C. Grönwall, and G. Tolt, "Continuously scanning time-correlated single-photon-counting single-pixel 3-d lidar," Opt. Eng. **56**, 031204–031213 (2016).
15. G. S. Buller, R. D. Harkins, A. McCarthy, P. A. Hiskett, G. R. MacKinnon, G. R. Smith, R. Sung, A. M. Wallace, R. A. Lamb, K. D. Ridley, and J. G. Rarity, "Multiple wavelength time-of-flight sensor based on time-correlated single-photon counting," Rev. Sci. Instrum. **76**, 083112 (2005).
16. N. J. Krichel, A. McCarthy, and G. S. Buller, "Resolving range ambiguity in a photon counting depth imager operating at kilometer distances," Opt. Express **18**, 9192–9206 (2010).
17. J. J. Degnan, "Photon-counting multikilohertz microlaser altimeters for airborne and spaceborne topographic measurements," J. Geodyn. **34**, 503–549 (2002).
18. P. Coates, "Analytical corrections for dead time effects in the measurement of time-interval distributions," Rev. Sci. Instrum. **63**, 2084–2088 (1992).
19. M. Patting, M. Wahl, P. Kapusta, and R. Erdmann, "Dead-time effects in tcspc data analysis," Proc. SPIE **6583**, 658307–658310 (2007).
20. J. W. Goodman, *Statistical Optics* (John Wiley & Sons, 2015).
21. G. R. Osche, *Optical Detection Theory for Laser Applications* (Wiley-Interscience, 2002).

22. D. G. Fouche, "Detection and false-alarm probabilities for laser radars that use geiger-mode detectors," Appl. Opt. **42**, 5388–5398 (2003).

23. Z. Li, J. Lai, C. Wang, W. Yan, and Z. Li, "Influence of dead-time on detection efficiency and range performance of photon-counting laser radar that uses a geiger-mode avalanche photodiode," Appl. Opt. **56**, 6680–6687 (2017).

24. M. Hayman and J. P. Thayer, "General description of polarization in lidar using stokes vectors and polar decomposition of mueller matrices," J. Opt. Soc. Am. A **29**, 400–409 (2012).

25. H. C. van de Hulst, *Light Scattering by Small Particles* (Courier Corporation, 1957).

26. M. Mishchenko and J. Hovenier, "Depolarization of light backscattered by randomly oriented nonspherical particles," Opt. Lett. **20**, 1356–1358 (1995).

27. C. J. Flynn, A. Mendoza, Y. Zheng, and S. Mathur, "Novel polarization-sensitive micropulse lidar measurement technique," Opt. Express **15**, 2785–2790 (2007).

28. G. G. Gimmestad, "Reexamination of depolarization in lidar measurements," Appl. Opt. **47**, 3795–3802 (2008).

29. S. Isbaner, N. Karedla, D. Ruhlandt, S. C. Stein, A. Chizhik, I. Gregor, and J. Enderlein, "Dead-time correction of fluorescence lifetime measurements and fluorescence lifetime imaging," Opt. Express **24**, 9429–9445 (2016).

30. S. E. Mitchell and J. P. Thayer, "Ranging through shallow semitransparent media with polarization lidar," J. Atmospheric Ocean. Technol. **31**, 681–697 (2014).

31. R. A. Stillwell, R. R. Neely III, J. P. Thayer, M. D. Shupe, and D. D. Turner, "Improved cloud-phase determination of low-level liquid and mixed-phase clouds by enhanced polarimetric lidar," Atmospheric Meas. Tech. **11**, 835–859 (2018).

32. J. M. Alvarez, M. A. Vaughan, C. A. Hostetler, W. H. Hunt, and D. M. Winker, "Calibration technique for polarization-sensitive lidars," J. Atmospheric Ocean. Technol. **23**, 683–699 (2006).

33. V. Freudenthaler, "About the effects of polarising optics on lidar signals and the delta-90 calibration," Atmos. Meas. Tech. **9**, 4181–4255 (2016).

34. J. D. Klett, "Stable analytical inversion solution for processing lidar returns," Appl. Opt. **20**, 211–220 (1981).

35. U. C. Herzfeld, B. W. McDonald, B. F. Wallin, T. A. Neumann, T. Markus, A. Brenner, and C. Field, "Algorithm for detection of ground and canopy cover in micropulse photon-counting lidar altimeter data in preparation for the icesat-2 mission," IEEE Trans. Geosci. Remote. Sens. **52**, 2109–2125 (2014).

36. W. J. Marais, R. E. Holz, Y. H. Hu, R. E. Kuehn, E. E. Eloranta, and R. M. Willett, "Approach to simultaneously denoise and invert backscatter and extinction from photon-limited atmospheric lidar observations," Appl. Opt. **55**, 8316–8334 (2016).

37. R. M. Willett and R. D. Nowak, "Multiscale poisson intensity and density estimation," IEEE Trans. Inf. Theory **53**, 3171–3187 (2007).

38. Z. T. Harmany, R. F. Marcia, and R. M. Willett, "This is spiral-tap: Sparse poisson intensity reconstruction algorithms - theory and practice," IEEE Trans. Image Process. **21**, 1084–1096 (2012).

39. D. M. Winker, M. A. Vaughan, A. Omar, Y. Hu, K. A. Powell, Z. Liu, W. H. Hunt, and S. A. Young, "Overview of the calipso mission and caliop data processing algorithms," J. Atmospheric Ocean. Technol. **26**, 2310–2323 (2009).

40. C. A. Hostetler, M. J. Behrenfeld, Y. Hu, J. W. Hair, and J. A. Schulien, "Spaceborne lidar in the study of marine systems," Ann. Rev. Mar. Sci. **10**, 121–147 (2018).